CHEMISTRY OF MATERIALS

Understanding the Formation of Colloidal Ferrimagnetic $CuCr_2Se_4$ Nanocrystals with Strong Room-Temperature Magnetic Circular Dichroism

Samantha Harvey, Jonathan M. DeStefano, Jiun-Haw Chu, Daniel R. Gamelin,* and Brandi M. Cossairt*

Cite This: *Chem. Mater.* 2024, 36, 10746−10757 **Read Online**

ACCESS | Metrics & More | Article Recommendations | Supporting Information

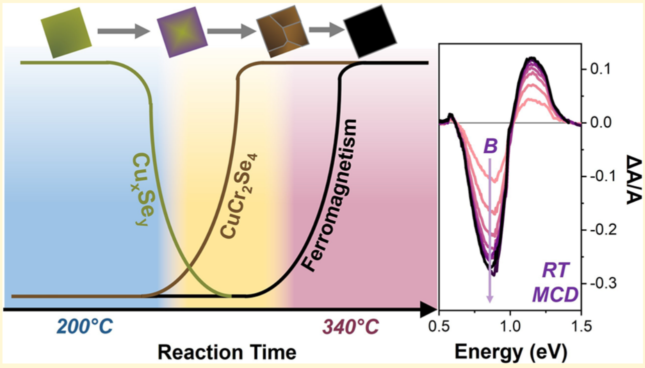

ABSTRACT: The ongoing development and eventual implementation of magnetic nanocrystals in devices requires not only syntheses that can bring bulk compositions down to the nanoscale but also a deep understanding of their formation such that size, morphology, and composition can be finely tuned. Chromium chalcogenide spinels are a class of materials that epitomize this dilemma; their unique magnetic and magneto-optical properties make them promising for applications in spintronics, data storage, and quantum information sciences, but only a few compositions have been synthesized as colloidal nanocrystals. Furthermore, these few existing reports lack mechanistic understanding and demonstrate little control over the physical characteristics of the final products. Here, we set forth to understand the synthesis of $CuCr_2Se_4$ nanocrystals by examining how the structure, composition, and magnetic properties evolve over the course of the reaction. We find that the material proceeds through binary copper selenide nanocrystal intermediates followed by Cr incorporation via diffusion. This process results in polycrystalline $CuCr_2Se_4$ nanocrystals that do not exhibit magnetic ordering until Cu incorporation modifies their stoichiometry and defects are annealed, which takes approximately 40 min at 340 °C to achieve. The resulting $CuCr_2Se_4$ nanocrystals show a strongly enhanced magnetic circular dichroism signal at the bulk plasma frequency of $\hbar\omega_{pl} \sim 1.0$ eV with a field dependence that reflects magnetization of the Cr^{3+} spin sublattice. These results highlight the possibility of solution processing strong near-IR magneto-optical materials for future device integration.

INTRODUCTION

Magnetic materials are critical components in a wide range of technologies, from spintronics (spin transistors, spin valves, logic switches, magnetic data storage)[1,2] to biomedicine (MRI contrast agents, magnetic heating).[3,4] When their magnetism is coupled with optical processes, this expands even further to include sensing,[5,6] magneto-optical memory,[7] and optical isolators.[8,9] With advances in technology, miniaturization has pushed the limits of common manufacturing techniques. Colloidal nanocrystals (NCs) offer a way toward solution processing of devices where suspensions can be spin-coated, drop-cast, or printed into precise configurations.[10−13]

Among the classes of materials that are optimal for the applications above, spinels are especially promising. Their composition (AB_2E_4, E = O, S, Se, Te) comprises both tetrahedrally coordinated divalent metals (A-site, e.g., Cu, Mn, Co, Fe, Zn, Cd, Hg, Mg) and octahedrally coordinated trivalent metals (B-site, e.g., Cr, Fe, Co, In, Al, V). The tunability of both metal sites introduces many unique properties, especially when one or both are occupied by magnetic cations.[14−16] While there are many types of magnetic ordering possible in these structures, most can be categorized as ferromagnets or ferrimagnets (magnetic A and B cations aligning antiferromagnetically).[14,17,18] Synthesis of these materials as NCs opens new avenues for modulating properties through size, shape, and heterostructures. Additionally, reducing the material's dimensionality down to the nanoscale may drastically alter magnetic properties, including the onset of superparamagnetism.

The promise of these compositions can be seen by looking at the oxide spinels, which have been most thoroughly investigated at the nanoscale. Numerous robust syntheses now exist that can produce monodisperse NCs with fine control over size and shape, along with complex core/shell heterostructures.[15,19−25] Some, like Fe_3O_4, have even been

Received: August 22, 2024
Revised: October 4, 2024
Accepted: October 7, 2024
Published: October 18, 2024

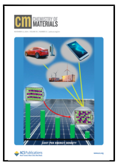

https://doi.org/10.1021/acs.chemmater.4c02365

commercialized for their magnetic properties.[26,27] On the other hand, research into chalcogenide spinel NCs has been lacking despite remarkable catalytic, magnetic, optical, and magneto-optical properties.[16,28] For example, the chromium chalcogenide compositions can exhibit multiferroicity ($CdCr_2S_4$, $CoCr_2S_4$, $FeCr_2E_4$, $MnCr_2S_4$),[14] colossal magnetoresistance ($FeCr_2S_4$),[29] colossal magnetocapacitance ($HgCr_2S_4$),[30] and have been proposed as cathode materials ($MgCr_2S_4$)[31] and photocatalysts ($ZnCr_2S_4$).[32] However, many have never been synthesized at the nanoscale, and those that have been reported lack control over size and morphology.[33−35]

Here, we focus on $CuCr_2Se_4$, a room-temperature ferrimagnet[36,37] with the highest Curie temperature among the chromium chalcogenide spinels at 430 K (157 °C).[38] The spin structure in $CuCr_2Se_4$ is best described by an antiferromagnetic interaction between Cr^{3+} and a delocalized hole in the Se 4p band, which gives rise to a net magnetic moment of $\sim 5\ \mu_B$ per formula unit.[36,39] Unlike many other spinel compositions, it is metallic with a bulk plasma frequency in the near-IR at $\hbar\omega_{pl} \sim 1.0$ eV that produces an extremely large magneto-optical Kerr rotation around −1.2° for single crystals at room temperature and a magnetic field of 0.25 T.[28,39−41] This proximity to the C-band telecommunication window makes $CuCr_2Se_4$ a promising material for Faraday isolators.[8] While there are existing reports of nanoscale $CuCr_2Se_4$, they offer conflicting results both with each other and with measurements of the bulk materials.[42−45] For example, Wang et al. reported that their 15−30 nm diameter $CuCr_2Se_4$ NCs were superparamagnetic,[43] while the 15−24 nm diameter NCs from Lin et al. were reported to be ferromagnetic with a T_C similar to bulk.[42] Furthermore, current syntheses result in high polydispersity and provide no *reliable* size and shape control, which makes correlating form with function difficult. With a clear understanding of how these NCs form, we will know which conditions to adjust to improve and eventually direct their structures. We may also be able to apply this knowledge to bring more spinels to the nanoscale.

Here, we delve into the synthesis of $CuCr_2Se_4$ NCs using powder X-ray diffraction (PXRD), inductively coupled plasma optical emission spectroscopy (ICP-OES), transmission electron microscopy (TEM), and magnetometry to better understand their formation as well as reconcile differences between existing preparations and bulk properties. We find that upon hot injection of the Cu/Cr precursor, copper selenide NCs form rapidly and serve as templates for the final spinel particles. As the temperature is maintained, Cr and Se begin to diffuse into the lattice, forming crystalline spinel domains around the edges. Upon raising the reaction temperature, incorporation is accelerated substantially, resulting in polycrystalline $CuCr_2Se_4$ particles. Despite forming the 1:2:4 crystal phase, room-temperature magnetic ordering is not present until after ~40 min at 340 °C, which we attribute to the annealing of grain boundaries and Cu incorporation. We frame these results in terms of the existing literature reports and suggest ways that the synthesis can be modified. Despite the unique near-IR magneto-optical properties of $CuCr_2Se_4$, absorptive measurements for NCs are lacking. We show that these NCs can be spin-coated as thin films to allow absorptive optical and magneto-optical characterization. Magnetic circular dichroism (MCD) measurements show a strong derivative-shaped signal centered around the bulk plasma frequency of $\hbar\omega_{pl} \sim 1.0$ eV.

■ EXPERIMENTAL METHODS

Chemicals. Chromium(III) chloride ($CrCl_3$, anhydrous, 99%) was purchased from Strem. Selenium powder (Se, 100 mesh, 99.99% trace), copper(I) chloride (CuCl, reagent grade, 99%), oleylamine (OLAm, >99% primary amine), and polydimethylsiloxane (PDMS, 200 fluid, viscosity 1000 cSt) were purchased from Sigma-Aldrich. CuCl was purified by dissolving in HCl and then using deionized water to precipitate. The solution was discarded, and the process was repeated a few times. The final pale solid was evacuated on a Schlenk line until dry, resulting in a fine white powder that was stored in a vial in an N_2 filled glovebox. Oleylamine was dried over CaH_2 overnight, distilled, and then stored over 3 Å sieves. All other chemicals were used as received without further purification.

Nanocrystal Synthesis. The synthesis described here was slightly modified from a previous report.[42] Glassware was dried at 160 °C overnight before being brought into an N_2 filled glovebox where all precursors were prepared. $CrCl_3$ (42 mg, 0.42 mmol), CuCl (133 mg, 0.84 mmol), and OLAm (9 mL) were added to a 15 mL 3-neck round-bottom flask along with T-adapter, thermowell, and rubber septum. Separately, Se (332 mg, 4.2 mmol) and OLAm (19 mL) were added to a 50 mL 3-neck round-bottom flask along with T-adapter, thermowell, and rubber septum. Flasks were sealed, brought out of the box, and placed on an N_2 Schlenk line. Tubing was cycled 3−5 times before opening the flasks to nitrogen. Under active nitrogen flow the T-adapter for the 50 mL flask was switched to a condenser. Both flasks underwent at least three evacuation-refill cycles to ensure all water and oxygen were removed. The flask containing Cu and Cr was heated to 150 °C for 15−30 min, giving a green solution. Short times (1−5 min) left $CrCl_3$ unreacted, while long times (>30 min) resulted in the formation of Cu^0 NCs (evident by the red color on the sides of the flask). The flask was removed from heat and cooled to 40 °C (the solution turned purple-gray). Meanwhile, the larger flask was kept at 340 °C for 15−30 min to dissolve Se. The solution changed color from yellow to red and was rapidly stirred to ensure reaction completion. The flask was then cooled to 200 °C. A 10 mL glass syringe was purged with nitrogen and then used to rapidly inject the Cu/Cr/OLAm mixture into the Se/OLAm solution. The reaction was maintained at 200 °C for 2 h. The temperature was then raised to 340 °C (~15 min) and was kept between 330 and 340 °C for up to 2 h. The reaction was stopped by removing the flask from the heating mantle. The particles were isolated via magnetic separation and washed with toluene. A few rounds of centrifugation (10 min, 7380 r.p.m.) with equal parts toluene and acetonitrile were also used.

Reaction aliquots (0.5−2.0 mL) were taken using an N_2-purged needle at set time points. Aliquots were rapidly injected into 3 mL of toluene in a centrifuge tube, sonicated, and then 7 mL of acetonitrile was added as antisolvent. Tubes were centrifuged at 10,000 r.p.m. for 5−10 min. Afterward, the supernatant was discarded, the NCs were redissolved in toluene, and the process was repeated once more.

ICP-OES. Solutions were pumped down under vacuum on a Schlenk line until ~2−20 mg of dried sample remained. Samples were digested overnight in 1 mL of 67% HNO_3 and 1 mL of H_2O_2. Afterward, 8 mL of 18 MΩ water was added, and the solutions were filtered using a nylon syringe filter. Stock solutions with Cu, Cr, and Se were used to generate calibration curves with correlation coefficients >0.999. Multiple emission lines for each element were used. A correction for the Se 203.985 line was calculated and is described in the Supporting Information (SI). All measurements were carried out on a PerkinElmer Optima 8300 Spectrophotometer.

X-ray Characterization. Silicon wafers were sonicated in toluene and acetone before drying in an oven at 160 °C. Samples were drop-cast in 5 μL increments, letting the spot dry completely between applications until enough material had been deposited that the silicon could no longer be seen. Powder X-ray diffraction (PXRD) patterns were collected on a Bruker D8 Discover diffractometer at 50 kV with 1000 μA via a Cu anode microfocus X-ray source ($\lambda = 1.5406$ Å) and a Pilatus 100 K large-area detector. The beam for the measurement was collimated to a diameter of 0.5 mm. X-ray photoelectron spectroscopy (XPS) data were taken on a Kratos Axis-Ultra DLD

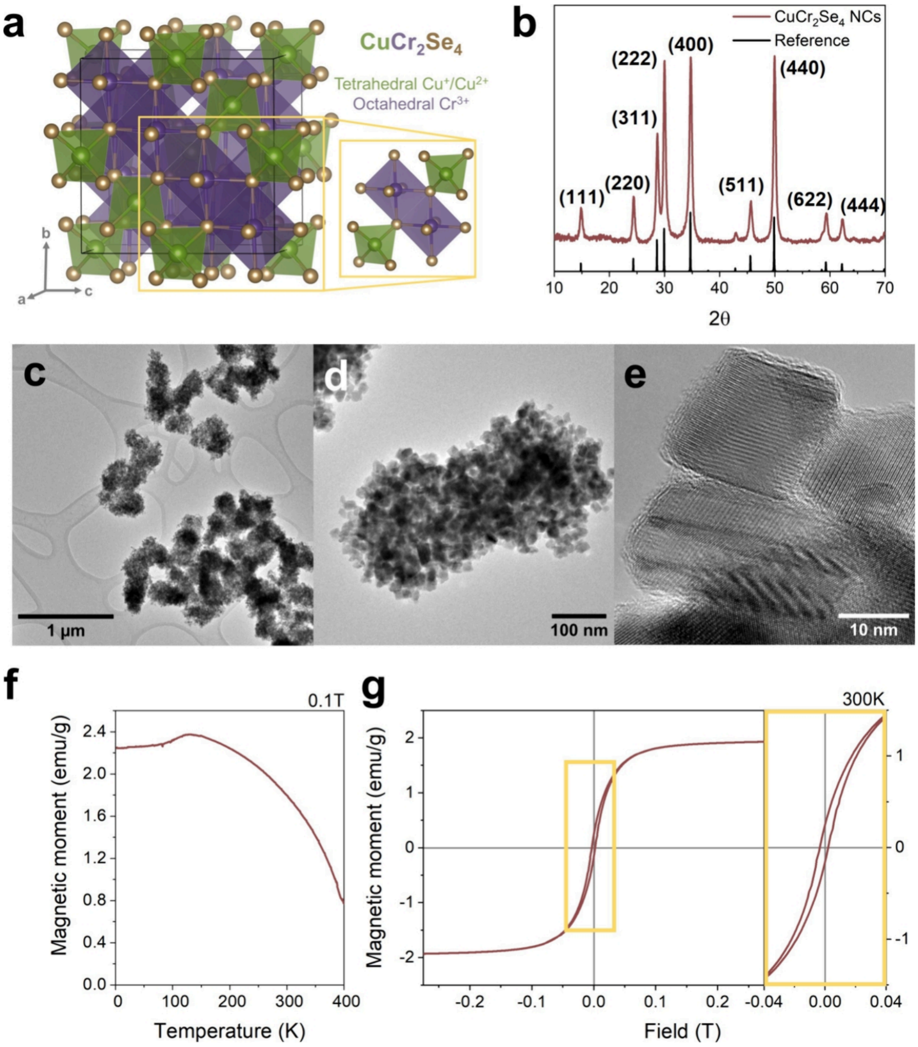

Figure 1. Characterization of $CuCr_2Se_4$ NCs. (a) Unit cell of $CuCr_2Se_4$ exhibiting the spinel crystal structure. The highlighted portion shows the tetrahedral and octahedral sites of copper and chromium, respectively. (b) PXRD pattern of the NCs with reference to ICSD 73403. (c−e) TEM images of magnetic aggregates and individual NCs. (f, g) Magnetic susceptibility measurements as a function of temperature (at 0.1 T) and field (at 300 K). The portion in yellow highlights the coercivity due to ferrimagnetic ordering.

spectrometer. This instrument has a monochromatized Al K-alpha X-ray source and a low-energy electron flood gun for charge neutralization. X-ray spot size for these acquisitions was on the order of 700 × 300 μm. The electrostatic lens was used for data collection. Pressure in the analytical chamber during spectral acquisition was less than 5×10^{-9} Torr. The pass energy for survey spectra (composition) was 160 eV. The pass energy for the high-resolution spectra was 40 eV. The takeoff angle (the angle between the sample normal and the input axis of the energy analyzer) was 0° (0-degree takeoff angle, ∼100 Å sampling depth). The Kratos Vision2 software program was used to determine peak areas and to calculate the elemental compositions from peak areas. CasaXPS was used to fit peaks in the high-resolution spectra. For the high-resolution spectra, a Shirley background was used, and all binding energies were referenced to the C ls signal of C−C bonds at 285.0 eV.

Electron Microscopy. Samples were diluted until color was barely visible, then 3 μL was drop-cast onto a TEM grid. Grids were dried overnight under vacuum to remove solvent. For transmission electron microscopy (TEM), we used ultrathin carbon with lacey carbon support on 400 mesh Cu grids, and for scanning transmission electron microscopy (STEM) and energy dispersive X-ray spectroscopy (EDS), we used ultrathin carbon with lacey carbon support on 300 mesh Au grids. Both types of grids were purchased from Ted Pella. TEM and STEM images were taken on a FEI Tecnai G2 F20 SuperTwin microscope operating at 200 kV. EDS data were collected with an Elite T EDAX detector.

Magnetic Measurements. Data were collected using a Quantum Design Physical Property Measurement System (PPMS-14T) via the vibrating sample magnetometry option. Dried powders were added to powder sample holders and inserted into brass half-tube sample holders for measurement. Magnetometry data was normalized to the mass of the dried powders.

Absorption Spectroscopy and Magnetic Circular Dichroism. Absorption spectra of reaction aliquots both before and after workup were measured in solution (Figure S20). All other optical characterization was done as thin films to reduce scattering from magnetic aggregation. NC films were prepared with a 1.5:1.0 w/w ratio of NCs and PDMS. To prepare a solution, 41.25 mg of $CuCr_2Se_4$ NCs was dissolved in 0.8 mL of toluene. Separately, 277.9 mg of PDMS was dissolved in 2.021 mL of toluene to form a stock solution. From this, 0.2 mL was added to the $CuCr_2Se_4$ solution. The sample was sonicated for an hour, followed by vortexing to ensure it was well mixed. When ready to spin-coat, the sample was kept in a sonicator for as long as possible before dispensing. 50 μL of the sample was pipetted onto a quartz disc and spin-coated at 1000 rpm for 30 s, followed by 4000 rpm for 30 s. The quartz disc (Infrasil, 0.5 in diameter, 1.0 mm thickness) was purchased from Thorlabs. Before spin-coating, it was cleaned via sonication with toluene, acetone, and hexanes. The absorption spectrum was collected on a Cary 5000 Spectrophotometer and background subtracted using a blank quartz disc. Magnetic circular dichroism (MCD) spectra were collected in the Faraday geometry using an Aviv 40DS spectropolarimeter, a GMW Model 3470 electromagnet, and either a Teledyne−Judson InGaAs detector (near-IR), a Hamamatsu R376 photocathode (visible), or a Hamamatsu R316-02 photocathode (visible to near-IR).

■ RESULTS AND DISCUSSION

$CuCr_2Se_4$ NCs were synthesized following an existing literature procedure with slight modifications (see Experimental Methods).[42] This synthesis results in NCs that crystallize in the spinel structure (Figure 1a), as evidenced by the PXRD pattern, which is plotted against a single crystal reference in Figure 1b.[46] Due to their magnetic ordering, the particles are prone to aggregation, as shown in the TEM images presented in Figure 1c,d. A high-resolution TEM (HR-TEM) image (Figure 1e) shows that the particles are highly crystalline. The NCs showed diameters of 18 ± 7 nm, and overall, the synthesis is robust, consistently producing average particle sizes of 16−24 nm. Vibrating sample magnetometry (VSM) data collected as a function of temperature and field (Figure 1f,g) are consistent with bulk magnetic data[28,38] as well as with that reported by Suzdalev and co-workers for NCs from whom the synthesis originated.[42] Their data also exhibited the anomalous feature around 140 K, which was attributed to nonstoichiometric amounts of selenium.[42] The low saturation field (∼0.1 T) and hysteresis in the room-temperature field-sweep data confirm the ferrimagnetic ordering. While we cannot determine the Curie temperature because of the limited temperature range of the measurement, we can determine that it is above 400 K, which puts it around the same value as bulk $CuCr_2Se_4$ (T_C = 430 K).

To understand how these NCs form, we took twenty-three aliquots over the course of a single reaction. Unless otherwise stated, each aliquot was purified by two rounds of precipitation via centrifugation and redispersion before characterization. The PXRD patterns for each are presented in Figure 2, along with the reference pattern for $CuCr_2Se_4$.[46] Immediately upon injection, we see the formation of crystalline features, which we attribute to copper selenide. The wide range of accessible Cu_xSe_y stoichiometries[47] can make identification difficult, and the formation of a mixture of phases in our synthesis further complicates this. The appearance of both triangular and cubic morphologies by TEM suggests both hexagonal and cubic crystal lattices.[48] Early time diffraction patterns are plotted against a variety of Cu_xSe_y phases in Figure S1 and align best with a mixture of cubic, hexagonal, and tetragonal $Cu_{2-x}Se$, hexagonal CuSe (klockmannite), and cubic Cu_3Se_2 (umangite). Fast Fourier transforms (FFTs) of TEM images from early time aliquots (200 °C, 10 or 20 min, Figure S2) show diffraction that can also be clearly assigned to four of these phases (See SI for more details). All of these phases have been shown to maintain Cu in its +1 oxidation state with changes to the Se oxidation state (−1 vs −2) and vacancies for charge compensation.[47] The preference for Cu^+-dominant phases is consistent with the reaction being run in oleylamine, which is known to be reducing and, therefore, prevents the formation of divalent copper despite the excess of Se in the reaction flask. Interestingly, Cu_3Se_2 can be derived from the $Cu_{1.8}Se$ phase via Cu rearrangement and lattice compression in the *c*-direction, but is also known to disproportionate into $Cu_{2-x}Se$ and CuSe above 135 °C.[47]

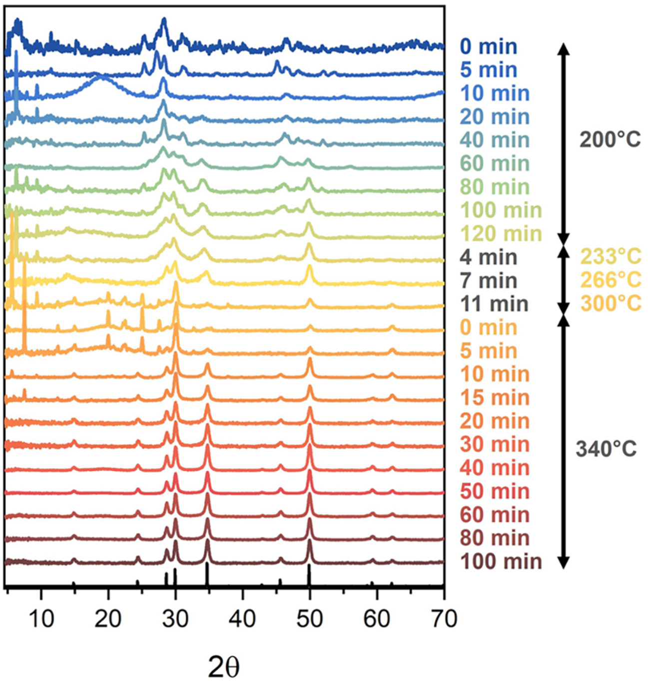

Figure 2. PXRD traces for aliquots taken during a single reaction. The reference pattern for $CuCr_2Se_4$ (ICSD 73403) is shown in black at the bottom.

The formation of binary Cu_xSe_y phases preceding the ternary $CuCr_2Se_4$ phase is not surprising; it has been shown that binary intermediates precede ternary nanomaterials in a variety of syntheses due to mismatch between the reactivity of the two metal precursors.[49] Copper chalcogenides are particularly well-known for forming rapidly, as has been shown for $CuInE_2$ (E = S, Se) NCs.[50−52] Chromium, on the other hand, reacts much slower and has been shown to require high temperatures and long reaction times to enter lattices, as was the case for $CrGeTe_3$ nanoplatelets.[53] A report by Buonsanti and co-workers that demonstrated the synthesis of $CuCrS_2$ NCs is particularly relevant.[54] In their case, intermediate Cu_xS (x = 1, 2) phases formed first, followed by $CuCrS_2$ after 5 h. Changing the Cu precursor from copper iodide to the more reactive copper acetate resulted in much faster formation of the ternary phase and no direct evidence of a binary intermediate. While this composition (S vs Se) and crystal structure (1:1:2 vs 1:2:4) differ from ours, this observation provides insight into the differences between the reported $CuCr_2Se_4$ NC syntheses, which often vary in both their Cu and Cr precursor choices.[42,43,55]

At around 80 min at 200 °C, we see broad $CuCr_2Se_4$ features appear by PXRD, which are due to small crystalline domains (Figure S5). As the temperature is increased and eventually reaches 340 °C, these features grow and narrow. No more changes are evident after 10 min at this elevated temperature, suggesting that the reaction has reached equilibrium, which, as will be shown below, is not the case.

Sharp, periodic features at low 2θ (5−10°) represent lamellar structures and persist until ∼10 min at 340 °C. Their lattice spacings are on the order of nanometers, which points to inorganic layers separated by oleylamine. These sheet structures can also be observed by TEM (Figure S7), persisting throughout the entire reaction. The lamellae are a mix of amorphous and crystalline segments, and FFTs of the latter provide lattice spacings that match the (111), (220), and (222) lattice planes of Cu_2Se (Figure S8). The formation of similar 2D morphologies has been noted at early time points in syntheses of Cu_2Se[56,57] and Cu[58] nanomaterials, arising from interactions between the metal salts and the aliphatic ligands. In fact, we see by PXRD the formation of lamellae in the Cu−Cr−OLAm reaction flask even prior to injection, which we hypothesize reflects the reaction of Cu ions with the oleylamine (Figure S9). The lowest 2θ peak gives a spacing of 1.48 nm, which increases to 1.56 nm after injection due to reaction with Se to form the 2D phase of Cu_2Se. At higher temperatures, more periodic features at slightly higher 2θ (20−30°) appear. These are known to also relate to 2D structures and are correlated with the degree of ordering between sheets.[59] We attribute the increase in these peaks in our system to the degradation of the lamellae, which enables more ordered stacking between the layers on smaller length scales.

To understand the atomic compositions of the aliquots, we performed elemental analysis with ICP-OES. The mole fractions of Cu, Cr, and Se as a function of reaction time are presented in Figure 3a. Horizontal lines denote the expected 1:2:4 stoichiometry. Figure 3b shows the same data but plotted as ratios, where the Cr and Se mole fractions are normalized against Cu. Dashed horizontal lines provide the Se:Cu ratios of common copper selenide phases. At early times, the system is dominated by copper and selenium, which is consistent with the PXRD patterns discussed above. The Cu:Se ratio follows a progression of increasing Se concentration from Cu_2Se to Cu_3Se_2 to CuSe, while the Cr:Cu ratio remains relatively consistent. As time progresses, the Cr mole fraction increases concurrently with Se, suggesting that the particles are enriching in Cr, but to do so, they must also bring in Se^{2-} to compensate for the Cr^{3+} charge. This trend continues as the temperature increases until at 340 °C, the stoichiometry is close to that of the 1:2:4 phase, which correlates with the dominant diffraction pattern of $CuCr_2Se_4$ observed by PXRD. However, the composition continues to evolve at 340 °C until ∼40 min later, it reaches a final composition that is deficient in Se. During this latter evolution, the Cr:Cu and Se:Cu ratios both decrease by ∼10%. Since the Cr:Cu and Se:Cu ratios in Figure 3b continue to overlap as they decrease, it is evident that either Cu is entering the lattice or both Cr^{3+} and Se^{2-} must be exiting. Because Cu^+ is highly mobile in crystalline lattices, we propose that these high temperatures promote incorporation and thereby modify the stoichiometry.[60] Given that the lamellae are also decomposing around this time, these copper-rich structures could serve as a reservoir of Cu cations.

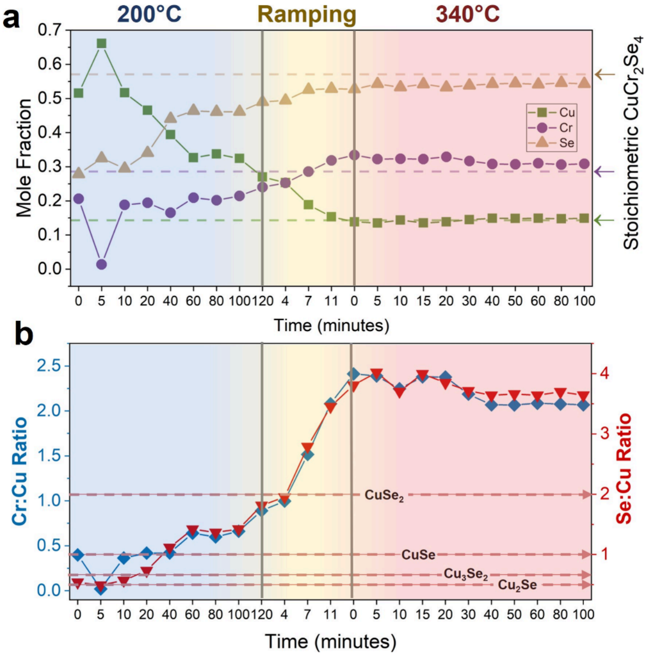

Figure 3. Elemental analysis of the reaction aliquots using ICP-OES. Different temperature regimes are highlighted: 200 °C in blue, ramping from 200 to 340 °C in yellow, and 340 °C in pink. (a) Mole fractions for Cu, Cr, and Se as a function of reaction time. The ratios for the stoichiometric 1:2:4 spinel structure are given by the dashed lines and arrows on the right *y*-axis. (b) Cr:Cu and Se:Cu mole-fraction ratios (where Cu is normalized to 1), plotted as a function of reaction time. The Se:Cu ratios of common copper selenide phases are provided as dashed red lines.

STEM-EDS mapping (Figure 4a−e) further confirms the incorporation of Cr at early times. The NCs exhibit an even distribution of selenium throughout their volume, but copper only occupies the core, while chromium is only present around the edges. Line scans (Figure S12) show that chromium is preferentially found at the NC edges but slowly moves into the core with time and temperature until Cu, Cr, and Se are all distributed uniformly (Figure S16). This process results in highly crystalline $CuCr_2Se_4$ domains that grow toward the NC center over time (Figure 4f,g). When these domains meet, they produce grain boundaries resulting in polycrystalline particles of $CuCr_2Se_4$. While these "picture frame" structures may appear hollow, which would suggest a Kirkendall effect of Cu diffusion outward while Cr diffuses in, we do not believe this is the case here. Instead, we attribute this to diffusion doping, which has been explored in Mn^{2+}-doped CdSe and related NCs.[61] Here, a bath of metal cations and excess chalcogens drive binding at the NC surfaces, and thermally activated solid-state diffusion eventually randomizes their positions throughout the entire NC lattice.[61] This process is accompanied by an increase in particle size, as observed in Figure S1 for the $CuCr_2Se_4$ NCs investigated here. This interpretation is confirmed by our STEM-EDS line scans, which do not show a diminishing Cu signal in the center of the NCs as Cr content increases (Figure S12). Instead of hollow structures, the contrast in bright-field TEM seen in Figure 4g can be attributed to the greater diffraction intensity of $CuCr_2Se_4$ compared to Cu_xSe_y.

Despite the formation of the 1:2:4 spinel phase by PXRD upon reaching 340 °C, the NCs are not yet magnetic enough to allow the room-temperature magnetic separation that is possible for the final product. A slow transition occurs from this "non-magnetic" state to one that exhibits ferrimagnetic ordering over 40 min. Coinciding with this change is an increase in aggregation due to interparticle magnetic attraction, as seen by scattering in the absorption spectra of the reaction aliquots (both before workup and after), along with particle clustering by TEM (Figures S18−S20). To determine if this change is due to a transition in magnetic ordering (e.g., superparamagnetic to ferromagnetic) or Curie temperature (i.e., T_C < 300 K to T_C = 430 K), we performed VSM measurements on NC aliquots taken before and after this transition. When compared to an aliquot collected at 100 min, the aliquot taken after only 10 min at 340 °C exhibits a much

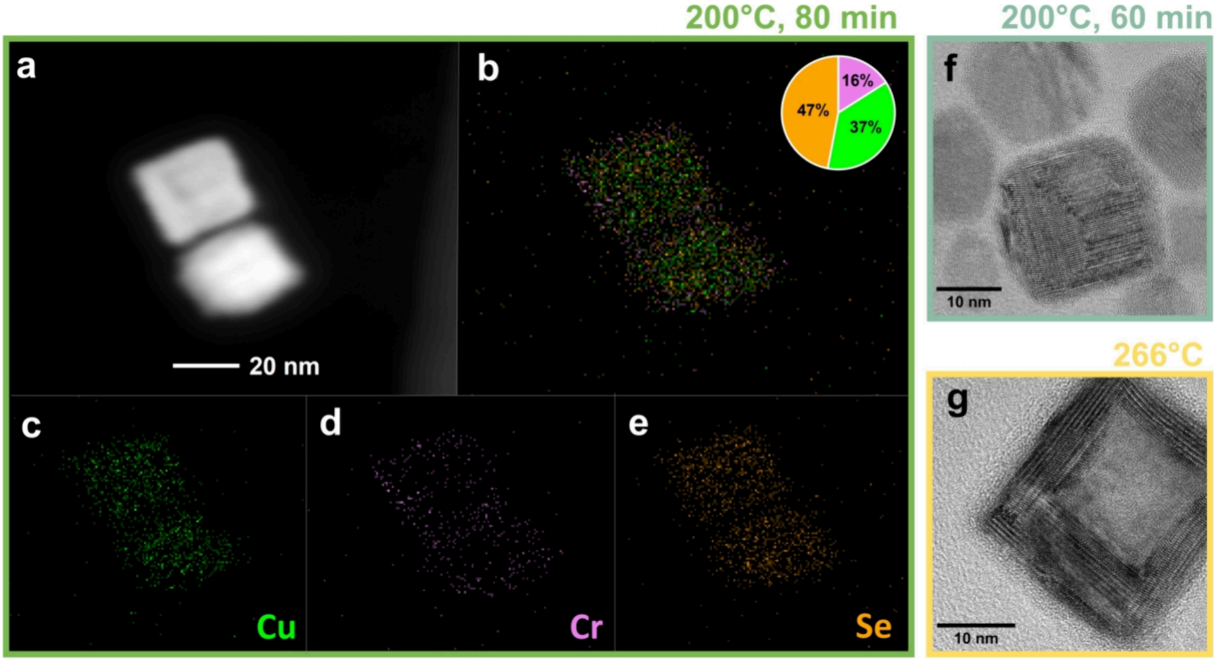

Figure 4. Cr incorporation into the nanocrystals at lower temperatures. (a−e) STEM-EDS mapping of a pair of nanocrystals showing Cr primarily on the edges of the copper selenide particles. (f, g) Bright-field HR-TEM images of particles showing multiple crystalline domains around the edges that cause polycrystalline structures.

smaller magnetic moment but similar temperature and field dependence (Figures 5a,b and normalized data, Figure S25). These results suggest that the NC ensemble effectively contains two populations: those that are magnetically ordered at high temperatures and those that show negligible magnetization at any temperature under our measurement conditions. The evolution in ensemble magnetism with reaction time is thus interpreted as arising from the slow conversion of weakly magnetic NCs into strongly magnetically ordered NCs until, eventually, every NC has been converted.

As shown in Figure 3 (and repeated in Figure 5c for the 340 °C portion of the reaction), the composition also continues to change for ∼40 min after reaching 340 °C. As discussed above, we attribute some of this change to the incorporation of Cu into the lattice to modify the stoichiometry. In the bulk, copper chromium chalcogenides are unique among the spinels as the A-site deviates from the expected 2+ oxidation state. Although debated for some time,[62−65] it is now accepted that these compositions have mostly monovalent Cu (with only about 7% divalent occupancy), trivalent chromium, and selenium vacancies for charge compensation.[36] This nonstoichiometry is what gives $CuCr_2E_4$ spinels their unique metallic, magnetic, and magneto-optical properties.[28,39] In our case, the NC lattice may need to convert into a similar off-stoichiometry to show ferrimagnetic ordering. From XPS (Figure S24), we can see that our final product also has mostly monovalent Cu (with ∼17% divalent).

When fitting the PXRD data for crystallite size through Scherrer analysis (Figure 5d) and for lattice parameters through peak position (Figure 5e), we see that this trend is repeated; the structure of the NCs continues to change up to ∼40 min at 340 °C. While at first glance it may seem that the NCs are growing, when particle size is determined by TEM image analysis, we find that despite a large standard deviation from polydispersity, the mean diameter is nearly constant throughout the entire reaction time at 340 °C. Given that the particles are polycrystalline, PXRD and TEM probe different characteristics; PXRD provides insight into crystalline *domain size* and TEM into *particle size*. As time progresses at 340 °C, the particles anneal and eliminate grain boundaries, increasing the domain size while maintaining the particle size. We attribute the change in lattice parameter to a distortion in the lattice that resolves itself after 40 min. While the root cause of this is still unknown, we can provide a few hypotheses that align with our results. The first is that the $CuCr_2Se_4$ lattice exhibits a tetragonal distortion that transitions into the more symmetric cubic structure with time.[66] This distortion could be due to grain boundaries in the polycrystalline particles, which disappear after annealing. A tetragonal distortion could also be associated with Jahn−Teller effects from a partial change in the average copper oxidation state from Cu^{2+} toward Cu^{+}.[14,67] It is also plausible that concurrent with the formation of $CuCr_2Se_4$ we have some portion of the 1:1:2 phase ($CuCrSe_2$) in our NCs. PXRD patterns of aliquots from 80 to 120 min do show some features that align with the 1:1:2 phase, although broadening and peak shifting preclude us from saying that it is a true intermediate (Figure S5). However, the 1:1:2 and the 1:2:4 phases exhibit very similar diffraction features with a notable shift to lower 2θ for the former.[43,46,68] Therefore, if we have a structure that is partway between these phases or if a minority of $CuCrSe_2$ lattices are present (either as separate NCs or as a domain within our particles), it could artificially shift our peaks and therefore our lattice parameter calculations. Importantly, the shifts would be more drastic for higher order peaks and would not affect features that do not have overlapping 1:1:2 peaks (e.g., 444), however this cannot be the only effect in play as it would cause all the peaks to shift to lower 2θ when we see shifting to both lower and higher 2θ (Figure S18). Regardless of whether distortions or phases cause this shift, it follows the same trend as our other measurements where changes are occurring until 40 min at 340 °C, pointing to a structural transition.

https://doi.org/10.1021/acs.chemmater.4c02365
Chem. Mater. 2024, 36, 10746−10757

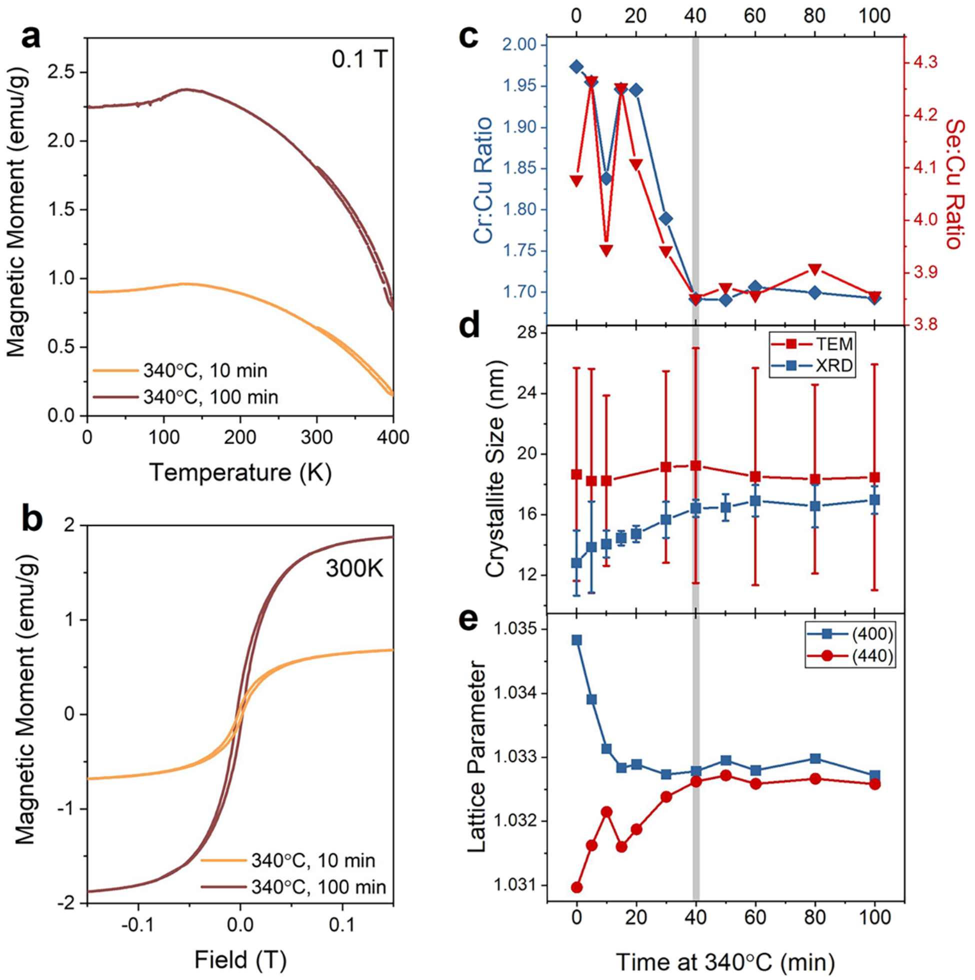

Figure 5. Transition to room-temperature ferrimagnetic ordering. (a, b) Magnetic susceptibility measurements on a NC aliquot taken after 10 min and after 100 min reaction time at 340 °C. (c) Elemental ratios of Cr:Cu and Se:Cu from ICP, plotted as a function of reaction time at 340 °C. Note that these data correspond to the 340 °C portion of the data shown in Figure 3b. (d) Crystallite size determined from Scherrer analysis of PXRD data and from analysis of TEM images. (e) Lattice parameters calculated from the peak positions of the (400) and (440) diffractions in PXRD. The gray line in figures (c−e) indicates the time by which all nanocrystals have transitioned.

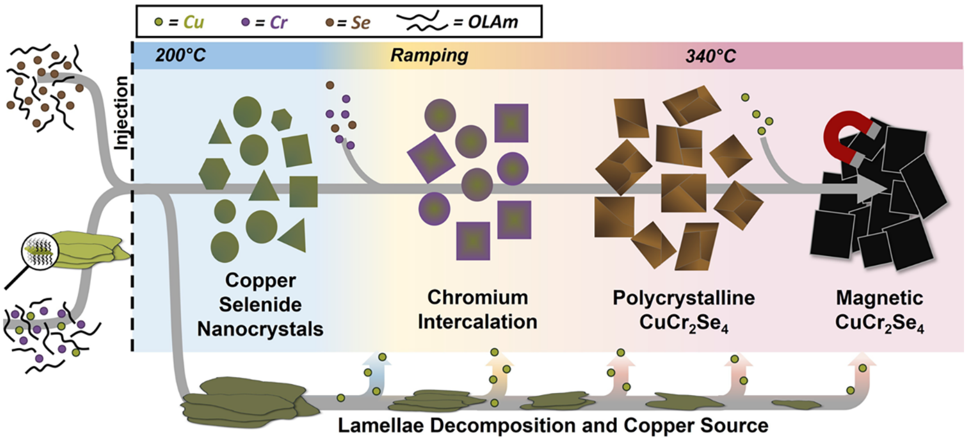

Figure 6. Mechanism for the formation of ferrimagnetic $CuCr_2Se_4$ nanocrystals.

Taken together, we can construct a mechanism for the formation of $CuCr_2Se_4$ NCs (Figure 6). The reaction begins with binary copper selenide NCs forming rapidly upon precursor injection, resulting in many Cu_xSe_y phases and particle sizes. After Cu_xSe_y NC formation, the slower reacting Cr then attaches to the exterior of these binary intermediates concurrently with Se to produce shells of $CuCr_2Se_4$ crystalline domains. As Cr incorporates into the lattice, these domains grow and spread toward the centers of the particles, eventually resulting in polycrystalline $CuCr_2Se_4$ NCs. High temperatures promote further Cu diffusion into the NCs and annealing of grain boundaries, which enable the NCs to transition into a ferrimagnetic phase. Copper also reacts with oleylamine prior to injection to form lamellae. Upon injection, these structures form Cu−Se lamellar byproducts that decompose throughout the reaction, serving as a reservoir for Cu ions.

With this in mind, we can reconcile differences between the previous reports of $CuCr_2Se_4$ NC syntheses. Wang et al. and Pang et al. ran their syntheses for less time, likely producing polycrystalline particles, which is consistent with their TEM images.[43,55] This, along with their choice of oxygen-containing Cu^{2+} salts, led to a stoichiometry of $CuCr_2Se_4$ that was not ferrimagnetic and instead exhibited superparamagnetic ordering. Lin et al., whose synthesis method we based this work on, mentioned that they could tune the size of their particles by changing how long the reaction was left at 340 °C. However, this sizing was determined by Scherrer analysis, which we found does not reflect the NC size but instead changes in crystallinity as the NCs are annealed. Furthermore, their reaction conditions required a minimum of 30 min at 340 °C, which coincides with the magnetic transitions we see at 40 min.[42] Since Cu_xSe_y NCs template the final form of the $CuCr_2Se_4$ NCs, it is likely that shape and size control will be limited by that of the binary intermediate. There is a great wealth of literature on the synthesis and morphological control of copper chalcogenide NCs that may translate well into the $CuCr_2Se_4$ system for size- and shape-control using a modified hot-injection synthesis.[47] Cu_xE_y nanomaterials have also been shown to readily undergo partial cation exchange to afford ternary materials such as $CuInE_2$ (E = S,Se) while maintaining the original morphology, which could open up new avenues for controlling composition in the copper chromium chalcogenide spinels.[69,70]

Given that bulk $CuCr_2Se_4$ has attractive magneto-optical properties in the near-IR, we wanted to ascertain whether $CuCr_2Se_4$ NCs show similar properties. Although a previous study[45] has reported MCD spectra of $Cu_{1-x}Fe_xCr_2Se_4$ NCs, data were collected only down to 1.2 eV (1033 nm), which is above the bulk plasma frequency ($\hbar\omega_{pl} \sim 1.0$ eV). For optical characterization, films were prepared by spin-coating solutions of NCs and polydimethylsiloxane (PDMS) in toluene onto quartz discs. The addition of PDMS was necessary to reduce aggregation of the NCs, and PDMS was chosen for its high transmittance across the visible and near-IR spectral ranges. Films prepared in this way are thus effectively frozen solutions of colloidal $CuCr_2Se_4$ NCs. These films are sufficiently transparent to allow absorption measurements of $CuCr_2Se_4$ throughout both the visible and near-IR, complementing the reflection data that have been reported for $CuCr_2Se_4$ single crystals. The room-temperature absorption spectrum of one such NC film is shown in Figure 7a and compared with literature reflectivity and optical conductivity data for bulk samples in Figure S29a,b. Although severely reduced by NC dispersion in PDMS, a relatively large scattering background from magnetic aggregation of the NCs is still observed. The spectrum is largely featureless, showing two maxima in the near-IR at around 0.6 and 1.2 eV. Optical conductivity spectra of bulk $CuCr_2Se_4$ exhibit a minimum at ∼1.0 eV (and a corresponding maximum in loss function), corresponding to the bulk plasma frequency.[39−41] Our NC films also exhibit a dip in absorption around 1.0 eV on top of a broad IR tail of unknown origin.

Room-temperature MCD spectra of the same NC film were collected at several different magnetic fields between ±0.2 T (Figure 7b). The MCD spectra show a prominent derivative-shaped feature centered at 1.02 eV, as well as a series of weaker overlapping features to higher energy. This MCD spectrum compares remarkably well with the magneto-optical Kerr rotation spectra of $CuCr_2Se_4$ single crystals, which are also dominated by a similar derivative feature centered at ∼1.0 eV (Figure S29c).[28,39,40] This MCD spectrum also compares well with the partial MCD spectrum of $CuCr_2Se_4$ NCs reported previously.[45] The features in the visible region are significantly less pronounced here than in either the previously reported NC MCD or bulk MOKE spectra, both of which were on much larger sized crystals (∼20−80 nm and >1 mm,

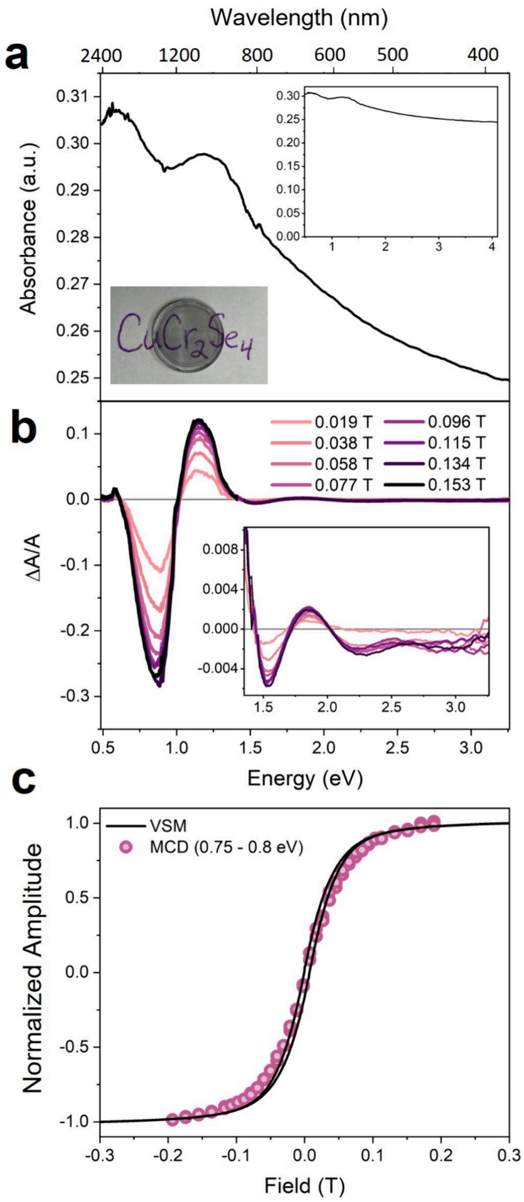

Figure 7. Magneto-optical characterization of $CuCr_2Se_4$ NCs. (a) Room-temperature absorption spectrum of a spin-coated NC film. The top inset shows a zoomed-out version of the same data, while the bottom inset shows a photograph of the sample. (b) Room-temperature MCD spectra of the same film collected at different magnetic field strengths. The inset shows the visible portion of the spectra in more detail. (c) Normalized 300 K magnetization curves obtained by integrating the MCD intensities at different fields between 0.75 and 0.80 eV. The solid curves show normalized 300 K magnetic susceptibility data for the same NCs obtained from VSM.

respectively). These higher-energy features have been attributed to a series of Cr^{3+} *d-d* and Se-to-Cr LMCT transitions.[39,71,72]

In bulk, the intense near-IR magneto-optical Kerr rotation has been identified as stemming from enhancement of the Kerr rotation of a dipole-allowed Cr^{3+}-to-Se(p) charge-transfer transition by the presence of the bulk plasma edge at the same frequency, $\hbar\omega_{pl}$.[28,39,40,71,73] Observation that the intense derivative MCD feature in ~18 nm diameter $CuCr_2Se_4$ NCs occurs at the same energy as the Kerr rotation in bulk $CuCr_2Se_4$ provides strong evidence that these NCs retain the high density of free carriers that makes the corresponding bulk material metallic. Using our analytical Cu^+ concentration, we calculate a carrier density of $P \sim 6.0 \times 10^{21}$ cm^{-3}, which is consistent with measurements on bulk $CuCr_2Se_4$ as well as with hole densities in other semimetallic copper chalcogenide NCs.[74−76] This MCD feature shifts to higher (lower) energy when chemical oxidants such as $NOBF_4$ (or reductant, cobaltocene) are added to the NC solution prior to film deposition (Figure S30), consistent with the expected $\sim P^{1/2}$ dependence of $\hbar\omega_{pl}$. This modulation of the MCD signal by carrier density engineering is reminiscent of results reported by Brändle et al., who showed that $CuCr_2Se_{3.7}Br_{0.3}$ single crystals exhibit red-shifted MOKE spectra. This result highlights that the carrier density (and therefore also the magneto-optical response) in $CuCr_2Se_4$ can be tuned not only through composition but also via postsynthetic redox titration of a type that is only achievable at the nanoscale. Overall, this large near-IR magneto-optical response means that these metallic $CuCr_2Se_4$ NCs retain the promising optical and magnetic properties of the bulk but are now solution-processable.

This plasma-enhanced near-IR MCD intensity is distinct from the plasmonic MCD features of metal and semimetal NCs described previously. The MCD spectra of plasmonic NCs based on nonmagnetic materials such as Ag, Au, ITO, ZnO, and $Cu_{2-x}Se$[77,78] all display derivative-shaped MCD signals associated with their localized surface plasmon resonances (LSPRs), but the 300 K rotational strengths ($\Delta A/A_{max}$) of those LSPRs are approximately 3 orders of magnitude smaller than the feature at ~1.0 eV in these $CuCr_2Se_4$ NCs under comparable measurement conditions. Additionally, whereas the LSPR MCD intensities of the plasmonic NCs mentioned above all stem predominantly from Landau splittings and are all therefore temperature independent and linearly dependent on applied magnetic field, the $CuCr_2Se_4$ NC MCD intensity tracks the magnetization of the Cr^{3+} spin sublattice (Figure 7c). The sign of the derivative MCD signal in these p-type $CuCr_2Se_4$ NCs is also opposite that expected from a Landau splitting of effective-mass holes based on carrier charge alone,[77] although in magnetic metals or semimetals, the total carrier effective-mass Hamiltonian has contributions from the Landau, Zeeman, and exchange-interaction Hamiltonians[79] and the LSPR temperature- and field-dependence may therefore deviate from this charge-only scenario, as reported recently for the MCD of paramagnetic Cu_5FeS_4 NCs.[80] The magneto-optical properties of ternary nanomaterials have drawn a lot of interest for their tunability, but also present very complex signatures due to the presence of mixed metal sites and oxidation states.[80−85] Overall, the data here indicate that colloidal ~18 nm diameter $CuCr_2Se_4$ NCs behave optically and magnetically like bulk $CuCr_2Se_4$, showing high-T_C magnetic ordering and huge enhancement of MCD intensities at the bulk plasma frequency. MCD intensity from this mechanism vastly exceeds the rotational strengths observed for LSPRs in colloidal semimetallic or metallic NCs. These findings are especially promising for applications such as solution-processed Faraday optical isolators, particularly as the MCD reported here is on par with or exceeds those of well-known magneto-optical and high Verdet constant materials such as yttrium iron garnet (YIG).[8,86−88]

CONCLUSIONS

$CuCr_2Se_4$ is known for having the highest Curie temperature among the chromium chalcogenide spinels and exhibiting a large magneto-optical signal in the near-IR. Although a few $CuCr_2Se_4$ NC syntheses have been reported, the conclusions were incongruent and occasionally deviated from expectations, given the material's bulk properties. We found that we could reconcile disparate prior results by examining the formation of $CuCr_2Se_4$ NCs in greater depth. Similar to many other ternary materials, $CuCr_2Se_4$ is found to form via binary intermediates, in this case, copper selenide NCs, that appear rapidly upon hot injection of precursors. These copper selenide NCs exist in a complex mixture of phases, resulting in size and shape polydispersity. The high mobility of Cu^+, which has often been exploited for cation exchange in other nanomaterials, likely allows the incorporation of the slower-reacting Cr species. As Cr^{3+} binds to the NC surfaces, it brings Se^{2-} along for charge compensation, forming $CuCr_2Se_4$ domains at the NC edges. Over time at elevated temperature, Cr^{3+} diffuses into the lattice, and these domains grow until they meet at the centers of the particles, yielding polycrystalline $CuCr_2Se_4$ NCs. At around 40 min at 340 °C, these particles undergo a transformation involving annealing grain boundaries along with further Cu incorporation fed by the decomposition of Cu_2Se lamellar side products. This unique formation process suggests that selective tuning of reaction parameters (injection/reaction temperature, precursors) may enable even finer control over the synthesis of nanocrystalline $CuCr_2Se_4$ by controlling the formation of the copper selenide phases. The single-crystalline $CuCr_2Se_4$ NCs prepared here exhibit high-temperature ferrimagnetic ordering analogous to bulk. MCD measurements on spin-coated thin films of these NCs show extremely large signals in the near-IR at the bulk plasma frequency, indicating retention of bulk-like metallicity and optical properties at the nanoscale. These NC MCD intensities track the magnetization of the Cr^{3+} spin sublattice, showing rapid saturation at low fields. These colloidal $CuCr_2Se_4$ NCs are thus potentially suitable for heterointegration strategies for introducing room-temperature magneto-optical functionality into next-generation photonics architectures.

ASSOCIATED CONTENT

Supporting Information

The Supporting Information is available free of charge at https://pubs.acs.org/doi/10.1021/acs.chemmater.4c02365.

> Determination of copper selenide phases, PXRD fits, additional TEM and STEM-EDS analysis, X-ray photoelectron data, carrier density calculations, redox modulation of MCD. This work was preprinted on ChemRxiv: DOI 10.26434/chemrxiv-2024-n2ktf (PDF)

AUTHOR INFORMATION

Corresponding Authors

Daniel R. Gamelin − *Department of Chemistry, University of Washington, Seattle, Washington 98195, United States;* orcid.org/0000-0003-2888-9916; Email: gamelin@uw.edu

Brandi M. Cossairt − *Department of Chemistry, University of Washington, Seattle, Washington 98195, United States;* orcid.org/0000-0002-9891-3259; Email: cossairt@uw.edu

Authors

Samantha Harvey − *Department of Chemistry, University of Washington, Seattle, Washington 98195, United States*

Jonathan M. DeStefano − *Department of Physics, University of Washington, Seattle, Washington 98195, United States;* orcid.org/0000-0002-7220-1261

Jiun-Haw Chu − *Department of Physics, University of Washington, Seattle, Washington 98195, United States*

Complete contact information is available at: https://pubs.acs.org/10.1021/acs.chemmater.4c02365

Notes

The authors declare no competing financial interest.

ACKNOWLEDGMENTS

This research was primarily supported by the U.S. National Science Foundation (NSF) through the UW Molecular Engineering Materials Center (MEM-C), a Materials Research Science and Engineering Center (Grant No DMR-2308979 to D.R.G., B.M.C., and J.-H.C.). S.M.H. was supported by the Intelligence Community Postdoctoral Research Fellowship Program at the University of Washington, administered by the Oak Ridge Institute for Science and Education (ORISE) through an interagency agreement between the U.S. Department of Energy and the Office of the Director of National Intelligence (ODNI). J.M.D. was supported by the National Science Foundation Graduate Research Fellowship Program under Grant No. DGE-2140004. Part of this work was conducted at the Molecular Analysis Facility, a National Nanotechnology Coordinated Infrastructure (NNCI) site at the University of Washington with partial support from the National Science Foundation via awards NNCI-1542101 and NNCI-2025489.

REFERENCES

(1) Hirohata, A.; Yamada, K.; Nakatani, Y.; Prejbeanu, I.-L.; Diény, B.; Pirro, P.; Hillebrands, B. Review on Spintronics: Principles and Device Applications. *J. Magn. Magn. Mater.* **2020**, *509*, No. 166711.

(2) Li, X.; Yang, J. First-Principles Design of Spintronics Materials. *National Science Review* **2016**, *3* (3), 365−381.

(3) Li, K.; Xu, J.; Li, P.; Fan, Y. A Review of Magnetic Ordered Materials in Biomedical Field: Constructions, Applications and Prospects. *Composites Part B: Engineering* **2022**, *228*, No. 109401.

(4) Martins, P. M.; Lima, A. C.; Ribeiro, S.; Lanceros-Mendez, S.; Martins, P. Magnetic Nanoparticles for Biomedical Applications: From the Soul of the Earth to the Deep History of Ourselves. *ACS Appl. Bio Mater.* **2021**, *4* (8), 5839−5870.

(5) Liu, C.; Shen, T.; Wu, H.-B.; Feng, Y.; Chen, J.-J. Applications of Magneto-Strictive, Magneto-Optical, Magnetic Fluid Materials in Optical Fiber Current Sensors and Optical Fiber Magnetic Field Sensors: A Review. *Optical Fiber Technology* **2021**, *65*, No. 102634.

(6) Chen, G.; Jin, Z.; Chen, J. A Review: Magneto-Optical Sensor Based on Magnetostrictive Materials and Magneto-Optical Material. *Sensors and Actuators Reports* **2023**, *5*, No. 100152.

(7) Kryder, M. H. Magneto-Optical Storage Materials. *Annu. Rev. Mater. Res.* **1993**, *23*, 411−436.

(8) Carothers, K. J.; Norwood, R. A.; Pyun, J. High Verdet Constant Materials for Magneto-Optical Faraday Rotation: A Review. *Chem. Mater.* **2022**, *34* (6), 2531−2544.

(9) Stadler, B. J. H.; Mizumoto, T. Integrated Magneto-Optical Materials and Isolators: A Review. *IEEE Photonics Journal* **2014**, *6* (1), 1−15.

(10) Akhavan, V. A.; Goodfellow, B. W.; Panthani, M. G.; Reid, D. K.; Hellebusch, D. J.; Adachi, T.; Korgel, B. A. Spray-Deposited $CuInSe_2$ Nanocrystal Photovoltaics. *Energy Environ. Sci.* **2010**, *3* (10), 1600−1606.

(11) Chen, Y.; Ryou, A.; Friedfeld, M. R.; Fryett, T.; Whitehead, J.; Cossairt, B. M.; Majumdar, A. Deterministic Positioning of Colloidal Quantum Dots on Silicon Nitride Nanobeam Cavities. *Nano Lett.* **2018**, *18* (10), 6404−6410.

(12) Eslamian, M. Inorganic and Organic Solution-Processed Thin Film Devices. *Nano-Micro Letters* **2017**, *9* (1), 3.

(13) Cohen, T. A.; Sharp, D.; Kluherz, K. T.; Chen, Y.; Munley, C.; Anderson, R. T.; Swanson, C. J.; De Yoreo, J. J.; Luscombe, C. K.; Majumdar, A.; Gamelin, D. R.; Mackenzie, J. D. Direct Patterning of Perovskite Nanocrystals on Nanophotonic Cavities with Electrohydrodynamic Inkjet Printing. *Nano Lett.* **2022**, *22* (14), 5681−5688.

(14) Tsurkan, V.; Krug von Nidda, H.-A.; Deisenhofer, J.; Lunkenheimer, P.; Loidl, A. On the Complexity of Spinels: Magnetic, Electronic, and Polar Ground States. *Phys. Rep.* **2021**, *926*, 1−86.

(15) Zhao, Q.; Yan, Z.; Chen, C.; Chen, J. Spinels: Controlled Preparation, Oxygen Reduction/Evolution Reaction Application, and Beyond. *Chem. Rev.* **2017**, *117* (15), 10121−10211.

(16) Ozel, F.; Kılıc, H. S.; Coskun, H.; Deveci, I.; Sarılmaz, A.; Balıkcıoglu, A.; Gundogdu, Y.; Aljabour, A.; Ozen, A.; Gezgin, S. Y.; Houimi, A.; Yar, A.; Kus, M.; Ersoz, M. A General Review on the Thiospinels and Their Energy Applications. *Materials Today Energy* **2021**, *21*, No. 100822.

(17) Sanchez-Lievanos, K. R.; Stair, J. L.; Knowles, K. E. Cation Distribution in Spinel Ferrite Nanocrystals: Characterization, Impact on Their Physical Properties, and Opportunities for Synthetic Control. *Inorg. Chem.* **2021**, *60* (7), 4291−4305.

(18) Jun, Y.; Seo, J.; Cheon, J. Nanoscaling Laws of Magnetic Nanoparticles and Their Applicabilities in Biomedical Sciences. *Acc. Chem. Res.* **2008**, *41* (2), 179−189.

(19) Kovalenko, M. V.; Bodnarchuk, M. I.; Lechner, R. T.; Hesser, G.; Schäffler, F.; Heiss, W. Fatty Acid Salts as Stabilizers in Size- and Shape-Controlled Nanocrystal Synthesis: The Case of Inverse Spinel Iron Oxide. *J. Am. Chem. Soc.* **2007**, *129* (20), 6352−6353.

(20) Rowell, J. L.; Jia, Y.; Shi, Z.; Molina Villarino, A.; Kang, M.; Yoon, D.; Jiang, K. Z.; Abruña, H. D.; Muller, D. A.; Robinson, R. D. General Route to Colloidally Stable, Low-Dispersity Manganese-Based Ternary Spinel Oxide Nanocrystals. *J. Am. Chem. Soc.* **2023**, *145* (31), 17406−17419.

(21) Liu, X.; Qiu, G.; Li, X. Shape-Controlled Synthesis and Properties of Uniform Spinel Cobalt Oxide Nanocubes. *Nanotechnology* **2005**, *16* (12), 3035.

(22) Song, Q.; Zhang, Z. J. Shape Control and Associated Magnetic Properties of Spinel Cobalt Ferrite Nanocrystals. *J. Am. Chem. Soc.* **2004**, *126* (19), 6164−6168.

(23) Sanchez-Lievanos, K. R.; Tariq, M.; Brennessel, W. W.; Knowles, K. E. Heterometallic Trinuclear Oxo-Centered Clusters as Single-Source Precursors for Synthesis of Stoichiometric Monodisperse Transition Metal Ferrite Nanocrystals. *Dalton Trans.* **2020**, *49* (45), 16348−16358.

(24) Sanna Angotzi, M.; Musinu, A.; Mameli, V.; Ardu, A.; Cara, C.; Niznansky, D.; Xin, H. L.; Cannas, C. Spinel Ferrite Core−Shell Nanostructures by a Versatile Solvothermal Seed-Mediated Growth Approach and Study of Their Nanointerfaces. *ACS Nano* **2017**, *11* (8), 7889−7900.

(25) Masala, O.; Hoffman, D.; Sundaram, N.; Page, K.; Proffen, T.; Lawes, G.; Seshadri, R. Preparation of Magnetic Spinel Ferrite Core/Shell Nanoparticles: Soft Ferrites on Hard Ferrites and Vice Versa. *Solid State Sci.* **2006**, *8* (9), 1015−1022.

(26) Wu, K.; Liu, J.; Saha, R.; Peng, C.; Su, D.; Wang, Y. A.; Wang, J.-P. Investigation of Commercial Iron Oxide Nanoparticles: Structural and Magnetic Property Characterization. *ACS Omega* **2021**, *6* (9), 6274−6283.

(27) Kralj, S.; Potrč, T.; Kocbek, P.; Marchesan, S.; Makovec, D. Design and Fabrication of Magnetically Responsive Nanocarriers for Drug Delivery. *Curr. Med. Chem.* **2017**, *24*, 454−469.

(28) Ohgushi, K.; Okimoto, Y.; Ogasawara, T.; Miyasaka, S.; Tokura, Y. Magnetic, Optical, and Magnetooptical Properties of Spinel-Type ACr_2X_4 (A = Mn, Fe, Co, Cu, Zn, Cd; X = O, S, Se). *J. Phys. Soc. Jpn.* **2008**, *77* (3), No. 034713.

(29) Ramirez, A. P.; Cava, R. J.; Krajewski, J. Colossal Magnetoresistance in Cr-Based Chalcogenide Spinels. *Nature* **1997**, *386* (6621), 156−159.

(30) Weber, S.; Lunkenheimer, P.; Fichtl, R.; Hemberger, J.; Tsurkan, V.; Loidl, A. Colossal Magnetocapacitance and Colossal Magnetoresistance in $HgCr_2Se_4$. *Phys. Rev. Lett.* **2006**, *96* (15), No. 157202.

(31) Wustrow, A.; Key, B.; Phillips, P. J.; Sa, N.; Lipton, A. S.; Klie, R. F.; Vaughey, J. T.; Poeppelmeier, K. R. Synthesis and Characterization of $MgCr_2S_4$ Thiospinel as a Potential Magnesium Cathode. *Inorg. Chem.* **2018**, *57* (14), 8634−8638.

(32) Yue, M.; Wang, R.; Cheng, N.; Cong, R.; Gao, W.; Yang, T. ZnCr2S4: Highly Effective Photocatalyst Converting Nitrate into N_2 without over-Reduction under Both UV and Pure Visible Light. *Sci. Rep.* **2016**, *6* (1), 30992.

(33) Pang, C.; Gao, L.; Singh, A. V.; Chen, H.; Bowman, M. K.; Bao, N.; Shen, L.; Gupta, A. Synthesis, Formation Mechanism, and Magnetic Properties of Monodisperse Semiconducting Spinel $CdCr_2S_4$ Nanocrystals via a Facile "Seed-Mediated" Growth Method. *Chem. Mater.* **2018**, *30* (5), 1701−1709.

(34) Mao, X.; Lee, J. Facile Synthesis of Phase-Pure $FeCr_2Se_4$ and $FeCr_2S_4$ Nanocrystals via a Wet Chemistry Method. *J. Mater. Chem. C* **2014**, *2* (19), 3744−3749.

(35) Malicka, E.; Karolus, M.; Groń, T.; Gudwański, A.; Ślebarski, A.; Goraus, J.; Oboz, M.; Sawicki, B.; Panek, J. Influence of Crystallite Size on the Magnetic Order in Semiconducting $ZnCr_2Se_4$ Nanoparticles. *Materials* **2019**, *12* (23), 3947.

(36) Kimura, A.; Matsuno, J.; Okabayashi, J.; Fujimori, A.; Shishidou, T.; Kulatov, E.; Kanomata, T. Soft X-Ray Magnetic Circular Dichroism Study of the Ferromagnetic Spinel-Type Cr Chalcogenides. *Phys. Rev. B* **2001**, *63* (22), No. 224420.

(37) Yamashita, O.; Yamauchi, H.; Yamaguchi, Y.; Watanabe, H. Magnetic Properties of the System $CuCr_2Se_{4\text{-}x}Y_x$ (Y = Cl, Br). *J. Phys. Soc. Jpn.* **1979**, *47* (2), 450−457.

(38) Nakatani, I.; Nosé, H.; Masumoto, K. Magnetic Properties of $CuCr_2Se_4$ Single Crystals. *J. Phys. Chem. Solids* **1978**, *39* (7), 743−749.

(39) Bordács, S.; Kézsmárki, I.; Ohgushi, K.; Tokura, Y. Experimental Band Structure of the Nearly Half-Metallic $CuCr_2Se_4$: An Optical and Magneto-Optical Study. *New J. Phys.* **2010**, *12* (5), No. 053039.

(40) Brändle, H.; Schoenes, J.; Wachter, P.; Hulliger, F.; Reim, W. Large Room-Temperature Magneto-Optical Kerr Effect in $CuCr_2Se_{4-x}Br_x$ (x = 0 and 0.3). *J. Magn. Magn. Mater.* **1991**, *93*, 207−210.

(41) Brändle, H.; Schoenes, J.; Wachter, P.; Hulliger, F.; Reim, W. Large Room-temperature Magneto-optical Kerr Effect in $CuCr_2Se_4$. *Appl. Phys. Lett.* **1990**, *56* (26), 2602−2603.

(42) Lin, C.-R.; Yeh, C.-L.; Lu, S.-Z.; Lyubutin, I. S.; Wang, S.-C.; Suzdalev, I. P. Synthesis, Characterization and Magnetic Properties of Nearly Monodisperse $CuCr_2Se_4$ Nanoparticles. *Nanotechnology* **2010**, *21* (23), No. 235603.

(43) Wang, Y.-H. A.; Bao, N.; Shen, L.; Padhan, P.; Gupta, A. Size-Controlled Synthesis of Magnetic $CuCr_2Se\ _4$ Nanocrystals. *J. Am. Chem. Soc.* **2007**, *129* (41), 12408−12409.

(44) Berends, A. C.; van der Stam, W.; Akkerman, Q. A.; Meeldijk, J. D.; van der Lit, J.; de Mello Donega, C. Anisotropic 2D $Cu_{2-x}Se$ Nanocrystals from Dodecaneselenol and Their Conversion to CdSe and $CuInSe_2$ Nanoparticles. *Chem. Mater.* **2018**, *30* (11), 3836−3846.

(45) Ivantsov, R. D.; Edelman, I. S.; Zharkov, S. M.; Velikanov, D. A.; Petrov, D. A.; Ovchinnikov, S. G.; Lin, C.-R.; Li, O.; Tseng, Y.-T. Effects of Processing Parameters on the Morphology, Structure, and Magnetic Properties of $Cu_{1-x}Fe_xCr_2Se_4$ Nanoparticles Synthesized with Chemical Methods. *J. Alloys Compd.* **2015**, *650*, 887−895.

(46) Okońska-Kozlowska, I.; Kopyczok, J.; Lutz, H. D.; Stingl, T. Single-Crystal Structure Refinement of Spinel-Type $CuCr_2Se_4$. *Acta Crystallographica Section C* **1993**, *49* (8), 1448−1449.

(47) Coughlan, C.; Ibáñez, M.; Dobrozhan, O.; Singh, A.; Cabot, A.; Ryan, K. M. Compound Copper Chalcogenide Nanocrystals. *Chem. Rev.* **2017**, *117* (9), 5865−6109.

(48) Boukouvala, C.; Daniel, J.; Ringe, E. Approaches to Modelling the Shape of Nanocrystals. *Nano Convergence* **2021**, *8* (1), 26.

(49) Lee, J. M.; Miller, R. C.; Moloney, L. J.; Prieto, A. L. The Development of Strategies for Nanoparticle Synthesis: Considerations for Deepening Understanding of Inherently Complex Systems. *J. Solid State Chem.* **2019**, *273*, 243−286.

(50) Yarema, O.; Yarema, M.; Wood, V. Tuning the Composition of Multicomponent Semiconductor Nanocrystals: The Case of I−III−VI Materials. *Chem. Mater.* **2018**, *30* (5), 1446−1461.

(51) Houck, D. W.; Nandu, S. V.; Siegler, T. D.; Korgel, B. A. $CuGaSe_2$ and $CuInxGa_{1-x}Se_2$ Nanocrystals with Sphalerite or Wurtzite Phase for Optoelectronic Applications. *ACS Appl. Nano Mater.* **2019**, *2* (7), 4673−4680.

(52) Tappan, B. A.; Barim, G.; Kwok, J. C.; Brutchey, R. L. Utilizing Diselenide Precursors toward Rationally Controlled Synthesis of Metastable $CuInSe_2$ Nanocrystals. *Chem. Mater.* **2018**, *30* (16), 5704−5713.

(53) Parobek, D.; DeLaney, C. R.; Watt, J.; Ivanov, S. A. Synthetic Understanding for Magnetic $CrGeTe_3$ Nanoplatelets. *Chem. Mater.* **2023**, *35*, 521.

(54) Mantella, V.; Varandili, S. B.; Pankhurst, J. R.; Buonsanti, R. Colloidal Synthesis of Cu−M−S (M = V, Cr, Mn) Nanocrystals by Tuning the Copper Precursor Reactivity. *Chem. Mater.* **2020**, *32* (22), 9780−9786.

(55) Pang, C.; Yang, R.; Singh, A.; Chen, H.; Bowman, M. K.; Bao, N.; Shen, L.; Gupta, A. Colloidal Synthesis and Magnetic Properties of Anisotropic-Shaped Spinel $CuCr_2Se_4$ Nanocrystals. *RSC Adv.* **2017**, *7* (50), 31173−31179.

(56) Hernández-Pagán, E. A.; Robinson, E. H.; La Croix, A. D.; Macdonald, J. E. Direct Synthesis of Novel $Cu_{2-x}Se$ Wurtzite Phase. *Chem. Mater.* **2019**, *31* (12), 4619−4624.

(57) Xie, Y.; Zheng, X.; Jiang, X.; Lu, J.; Zhu, L. Sonochemical Synthesis and Mechanistic Study of Copper Selenides $Cu_{2\text{-}x}Se$, β-CuSe, and Cu_3Se_2. *Inorg. Chem.* **2002**, *41* (2), 387−392.

(58) Pankhurst, J. R.; Castilla-Amorós, L.; Stoian, D. C.; Vavra, J.; Mantella, V.; Albertini, P. P.; Buonsanti, R. Copper Phosphonate Lamella Intermediates Control the Shape of Colloidal Copper Nanocrystals. *J. Am. Chem. Soc.* **2022**, *144* (27), 12261−12271.

(59) Toso, S.; Baranov, D.; Filippi, U.; Giannini, C.; Manna, L. Collective Diffraction Effects in Perovskite Nanocrystal Superlattices. *Acc. Chem. Res.* **2023**, *56* (1), 66−76.

(60) Schaak, R. E.; Steimle, B. C.; Fenton, J. L. Made-to-Order Heterostructured Nanoparticle Libraries. *Acc. Chem. Res.* **2020**, *53* (11), 2558−2568.

(61) Vlaskin, V. A.; Barrows, C. J.; Erickson, C. S.; Gamelin, D. R. Nanocrystal Diffusion Doping. *J. Am. Chem. Soc.* **2013**, *135* (38), 14380−14389.

(62) Colominas, C. Neutron-Diffraction Investigation of $CuCr_2Se_4$ and $CuCr_2Te_4$. *Phys. Rev.* **1967**, *153* (2), 558−560.

(63) Lotgering, F. K.; van Stapele, R. P. Magnetic and Electrical Properties of Copper Containing Sulphides and Selenides with Spinel Structure. *Solid State Commun.* **1967**, *5* (2), 143−146.

(64) Sleight, A. W. Cu^{+2} or Cu^{+1} in Chalcogenide Spinels? *Mater. Res. Bull.* **1967**, *2* (12), 1107−1109.

(65) Hollander, J. C. Th.; Sawatzky, G.; Haas, C. Monovalent Copper in the Chalcogenide Spinel $CuCr_2Se_4$. *Solid State Commun.* **1974**, *15* (4), 747−751.

(66) Bettinger, J. S.; Chopdekar, R. V.; Liberati, M.; Neulinger, J. R.; Chshiev, M.; Takamura, Y.; Alldredge, L. M. B.; Arenholz, E.; Idzerda, Y. U.; Stacy, A. M.; Butler, W. H.; Suzuki, Y. Magnetism and Transport of $CuCr_2Se_4$ Thin Films. *J. Magn. Magn. Mater.* **2007**, *318* (1), 65−73.

(67) Kyono, A.; Gramsch, S. A.; Nakamoto, Y.; Sakata, M.; Kato, M.; Tamura, T.; Yamanaka, T. High-Pressure Behavior of Cuprospinel $CuFe_2O_4$: Influence of the Jahn-Teller Effect on the Spinel. *Structure.* **2015**, *100* (8−9), 1752−1761.

(68) Suprenenko, P. A.; Kal'naya, G. I.; Murashko, N. I.; Obolonchik, V. A. Magnetic Susceptibility of Ternary Chromium Chalcogenides. *Inorg. Mater.* **1974**, *10* (6), 980−982.

(69) van der Stam, W.; Berends, A. C.; Rabouw, F. T.; Willhammar, T.; Ke, X.; Meeldijk, J. D.; Bals, S.; de Mello Donega, C. Luminescent CuInS2 Quantum Dots by Partial Cation Exchange in $Cu_{2-x}S$ Nanocrystals. *Chem. Mater.* **2015**, *27* (2), 621−628.

(70) van der Stam, W.; Bladt, E.; Rabouw, F. T.; Bals, S.; de Mello Donega, C. Near-Infrared Emitting $CuInSe_2/CuInS_2$ Dot Core/Rod Shell Heteronanorods by Sequential Cation Exchange. *ACS Nano* **2015**, *9* (11), 11430−11438.

(71) Antonov, V. N.; Antropov, V. P.; Harmon, B. N.; Yaresko, A. N.; Perlov, A. Ya. Fully Relativistic Spin-Polarized LMTO Calculations of the Magneto-Optical Kerr Effect of d and f Ferromagnetic Materials. I. Chromium Spinel Chalcogenides. *Phys. Rev. B* **1999**, *59* (22), 14552−14560.

(72) Saha-Dasgupta, T.; De Raychaudhury, M.; Sarma, D. D. Ferromagnetism in Metallic Chalcospinels $CuCr_2S_4$ and $CuCr_2Se_4$. *Phys. Rev. B* **2007**, *76* (5), No. 054441.

(73) Feil, H.; Haas, C. Magneto-Optical Kerr Effect, Enhanced by the Plasma Resonance of Charge Carriers. *Phys. Rev. Lett.* **1987**, *58* (1), 65−68.

(74) Marbella, L. E.; Gan, X. Y.; Kaseman, D. C.; Millstone, J. E. Correlating Carrier Density and Emergent Plasmonic Features in $Cu_{2-x}Se$ Nanoparticles. *Nano Lett.* **2017**, *17* (4), 2414−2419.

(75) Luther, J. M.; Jain, P. K.; Ewers, T.; Alivisatos, A. P. Localized Surface Plasmon Resonances Arising from Free Carriers in Doped Quantum Dots. *Nat. Mater.* **2011**, *10* (5), 361−366.

(76) Lee, W.-L.; Watauchi, S.; Miller, V. L.; Cava, R. J.; Ong, N. P. Dissipationless Anomalous Hall Current in the Ferromagnetic Spinel $CuCr_2Se_{4-x}Br_x$. *Science* **2004**, *303* (5664), 1647−1649.

(77) Hartstein, K. H.; Schimpf, A. M.; Salvador, M.; Gamelin, D. R. Cyclotron Splittings in the Plasmon Resonances of Electronically Doped Semiconductor Nanocrystals Probed by Magnetic Circular Dichroism Spectroscopy. *J. Phys. Chem. Lett.* **2017**, *8* (8), 1831−1836.

(78) Pineider, F.; Campo, G.; Bonanni, V.; de Julián Fernández, C.; Mattei, G.; Caneschi, A.; Gatteschi, D.; Sangregorio, C. Circular Magnetoplasmonic Modes in Gold Nanoparticles. *Nano Lett.* **2013**, *13* (10), 4785−4789.

(79) Khodaparast, G. A.; Matsuda, Y. H.; Saha, D.; Sanders, G. D.; Stanton, C. J.; Saito, H.; Takeyama, S.; Merritt, T. R.; Feeser, C.; Wessels, B. W.; Liu, X.; Furdyna, J. Cyclotron Resonance in Ferromagnetic InMnAs and InMnSb. *Phys. Rev. B* **2013**, *88* (23), No. 235204.

(80) Kuszynski, J. E.; Kays, J. C.; Conti, C. R. I.; McGill, S. A.; Dennis, A. M.; Strouse, G. F. Effective Mass for Holes in Paramagnetic, Plasmonic Cu_5FeS_4 Semiconductor Nanocrystals. *J. Phys. Chem. C* **2022**, *126* (30), 12669−12679.

(81) Kenny-Wilby, A.; Jaics, G.; Zhang, C.; Yin, P.; Radovanovic, P. V. Revisiting Plasmonic Properties of Complex Semiconductor Nanocrystals Using Magnetic Circular Dichroism Spectroscopy: A Cautionary Tale. *J. Phys. Chem. C* **2023**, *127* (2), 1087−1096.

(82) Kitagawa, Y.; Yao, H. Plasmon-Induced Polarity Inversion of Magnetic Circular Dichroism (MCD) Responses of Cu−Fe−S Bornite Nanodots upon Oxidation. *J. Phys. Chem. C* **2023**, *127* (45), 22149−22156.

(83) Yao, Y.; Bhargava, A.; Robinson, R. D. Fe Cations Control the Plasmon Evolution in $CuFeS_2$ Nanocrystals. *Chem. Mater.* **2021**, *33* (2), 608−615.

(84) Urso, C.; Barawi, M.; Gaspari, R.; Sirigu, G.; Kriegel, I.; Zavelani-Rossi, M.; Scotognella, F.; Manca, M.; Prato, M.; De Trizio, L.; Manna, L. Colloidal Synthesis of Bipolar Off-Stoichiometric Gallium Iron Oxide Spinel-Type Nanocrystals with Near-IR Plasmon Resonance. *J. Am. Chem. Soc.* **2017**, *139* (3), 1198−1206.

(85) Zhong, Y.; Liu, Z.; Sarnello, E.; Li, T.; Liu, Y.; Chen, J.; Ye, X. Controlling Infrared Plasmon Resonances in Inverse-Spinel Cadmium Stannate Nanocrystals via Site-Selective Cation-Exchange Reactions. *Chem. Mater.* **2021**, *33* (6), 1954−1963.

(86) Dillon, J. F. Magnetic and Optical Properties of Rare Earth Garnets. *J. Magn. Magn. Mater.* **1990**, *84* (3), 213−221.

(87) Scott, G. B.; Lacklison, D. E.; Ralph, H. I.; Page, J. L. Magnetic Circular Dichroism and Faraday Rotation Spectra of $Y_3Fe_5O_{12}$. *Phys. Rev. B* **1975**, *12* (7), 2562−2571.

(88) Canit, J. C.; Badoz, J.; Briat, B.; Krishnan, R. Magnetic Circular and Linear Dichroism of Iron Garnets Thin Films. *Solid State Commun.* **1974**, *15* (4), 767−770.